MicroED structure of the human adenosine receptor determined from a single nanocrystal in LCP

Michael W. Martynowycz[a,b], Anna Shiriaeva[c,d], Xuanrui Ge[c,e], Johan Hattne[a,b], Brent L. Nannenga[f,g], Vadim Cherezov[c,d,1], and Tamir Gonen[a,b,h,1]

[a]HHMI, University of California, Los Angeles, CA 90095; [b]Department of Biological Chemistry, University of California, Los Angeles, CA 90095; [c]Bridge Institute, University of Southern California Michelson Center for Convergent Biosciences, University of Southern California, Los Angeles, CA 90007; [d]Department of Chemistry, University of Southern California, Los Angeles, CA 90007; [e]Mork Family Department of Chemical Engineering and Materials Science, University of Southern California, Los Angeles, CA 90007; [f]Chemical Engineering, School for Engineering of Matter, Transport, and Energy, Arizona State University, Tempe, AZ 85287; [g]Biodesign Center for Applied Structural Discovery, Biodesign Institute, Arizona State University, Tempe, AZ 85287; and [h]Department of Physiology, University of California, Los Angeles, CA 90095

Edited by Yifan Cheng, University of California, San Francisco, CA, and approved July 20, 2021 (received for review March 29, 2021)

G protein–coupled receptors (GPCRs), or seven-transmembrane receptors, are a superfamily of membrane proteins that are critically important to physiological processes in the human body. Determining high-resolution structures of GPCRs without bound cognate signaling partners, such as a G protein, requires crystallization in lipidic cubic phase (LCP). GPCR crystals grown in LCP are often too small for traditional X-ray crystallography. These microcrystals are ideal for investigation by microcrystal electron diffraction (MicroED), but the gel-like nature of LCP makes traditional approaches to MicroED sample preparation insurmountable. Here, we show that the structure of a human A_{2A} adenosine receptor can be determined by MicroED after converting the LCP into the sponge phase followed by focused ion-beam milling. We determined the structure of the A_{2A} adenosine receptor to 2.8-Å resolution and resolved an antagonist in its orthosteric ligand-binding site, as well as four cholesterol molecules bound around the receptor. This study lays the groundwork for future structural studies of lipid-embedded membrane proteins by MicroED using single microcrystals that would be impossible with other crystallographic methods.

MicroED | membrane proteins | GPCR | ion-beam milling | lipidic cubic phase

G protein–coupled receptors (GPCRs) constitute a large and highly diverse membrane protein superfamily in the human genome represented by over 800 members (1, 2). Expressed on the cell surface plasma membrane, receptors function as cellular gatekeepers, transmitting signals inside the cell in response to a variety of signaling molecules and environmental cues. GPCR-mediated signaling pathways play a key role in all vital physiological systems, as well as pathophysiological conditions, including cancer, cardiovascular diseases, immune and metabolic disorders, pain and addiction, and others (3). Because of their fundamental roles in health and disease, GPCRs have been recognized as important drug targets, with over 30% of all approved therapeutic drugs acting via these receptors (4).

Adenosine A_{2A} receptor (A_{2A}AR) is prototypical and one of the most extensively studied GPCRs (5). It expresses broadly in the central nervous system and peripheral tissues and responds to an extracellular neuromodulator adenosine, mediating a range of physiological processes, including sleep regulation, angiogenesis, and immunosuppression. A_{2A}AR agonists are used clinically in pharmacological stress testing because of their vasodilatory effects (5). Antagonists have been considered as potential candidates for the treatment of Parkinson's disease and other neurodegenerative disorders (6), as well as, more recently, promising agents for cancer immunotherapy (7).

Structure-based drug discovery and optimization require accurate atomic models (8, 9). Recent advances in single particle analysis using cryogenic electron microscopy (cryo-EM) have allowed for high-resolution structures of several GPCRs to be determined, most of which have been obtained in complex with the G protein because of the size limitations in single particle analysis (10, 11). Nevertheless, crystallography remains the only approach of studying the receptors in their inactive state, without a bound signaling partner, in complex with antagonists or inverse agonists. The majority of GPCR structures have been determined using crystallization in a lipidic cubic phase (LCP) (12, 13).

Determining GPCR structures using traditional X-ray crystallography is challenging. Extracting crystals from the viscous LCP is difficult, and many membrane protein crystals only grow to a few micrometers in their largest dimension. Even when relatively large crystals are available, soaking drugs into them is not always feasible, limiting structure-based drug discovery applications for GPCRs (14). Therefore, structural investigations of GPCRs were greatly facilitated by the advent of X-ray free electron lasers (XFEL) with injector-based LCP delivery systems (10, 15, 16). These approaches took many years to develop, XFEL sources are costly, and access is highly competitive. Furthermore, millions of individual crystals are typically used during an XFEL experiment, and data from several thousands are then merged to generate a structure. For these reasons we explored the use of the relatively new microcrystal electron diffraction (MicroED) method for determining the structure of a GPCR from crystals grown in LCP.

MicroED is ideally suited to study protein nanocrystals of soluble proteins (17–19), membrane proteins (20–22), and small molecules

Significance

Microcrystal electron diffraction (MicroED) is a cryogenic electron microscopy (cryo-EM) method that determines protein structures from submicron crystals. G protein–coupled receptors (GPCRs) are membrane proteins that are critically important drug targets. These proteins require crystallization in lipidic cubic phase (LCP), making standard MicroED approaches intractable for investigating these samples. Here, we show that GPCR microcrystals grown in an LCP can be made amenable for MicroED by converting the LCP to the sponge phase and then ion-beam milling the crystals into thin lamellae. Our findings provide the basis for solving GPCR structures using MicroED, with future applications in structure-based drug discovery.

Author contributions: M.W.M., V.C., and T.G. designed research; M.W.M., A.S., X.G., J.H., B.L.N., V.C., and T.G. performed research; V.C. contributed new reagents/analytic tools; M.W.M., A.S., X.G., J.H., V.C., and T.G. analyzed data; and M.W.M., J.H., B.L.N., V.C., and T.G. wrote the paper.

The authors declare no competing interest.

This article is a PNAS Direct Submission.

[1]To whom correspondence may be addressed. Email: cherezov@usc.edu or tgonen@g.ucla.edu.

This article contains supporting information online at https://www.pnas.org/lookup/suppl/doi:10.1073/pnas.2106041118/-/DCSupplemental.

Published August 30, 2021.

(19, 23–25). However, recent investigations attempting to extract crystals from the viscous lipid-matrix have demonstrated that traditional sample preparation methods are ill-equipped to isolate well-diffracting crystals for MicroED experiments (26, 27). Clearly, further important improvements were required to make GPCR crystals grown in LCP amenable to MicroED analyses.

Here, we combine cryogenic focused ion-beam (FIB) milling with MicroED to determine the structure of the GPCR $A_{2A}AR$ embedded in LCP from a single microcrystal. To facilitate crystallization, the $A_{2A}AR$ was fused with apocytochrome $b_{562}RIL$ into its third intracellular loop, and its C-terminal residues 317 to 412 were truncated ($A_{2A}AR$-BRIL-ΔC, hereafter $A_{2A}AR$) (28). In order to deposit a thin layer of lipid matrix containing GPCR crystals onto a transmission electron microscope (TEM) grid, the gel-phased LCP was converted to the liquid-like sponge phase by mixing the LCP with a sponge phase-inducing agent (29). Only after LCP conversion into the sponge phase, blotting away the excess material, and FIB milling crystals into thin lamellae, were we able to collect continuous rotation MicroED data and determine the high-resolution structure.

Results and Discussion

Several methods for grid preparation were attempted before well-diffracting crystals were obtained. In a recent report we demonstrated that mammalian voltage-dependent anion channel (mVDAC) crystals grown in the presence of lipid bicelles were amenable to FIB milling and subsequent structure determination by MicroED when crystals were transferred onto a TEM grid at high humidity (22). Although we attempted direct transfer of $A_{2A}AR$ crystals grown in LCP, that strategy did not yield satisfactory results. This is likely because the LCP is more viscous and difficult to spread out in a thin layer compared with a bicellar preparation. With extensive trial and error, we succeeded in transferring crystals onto grids, but ultimately it resulted in poor diffraction (Fig. 1*A* and *SI Appendix*, Figs. S1 and S2). The lipidic mesophase surrounding the crystals appeared to be clumped and exposed parts of the crystal to the air. Most likely, the sample dehydrated during the transfer changed the concentrations of ingredients in the crystallization mixture and potentially transformed the LCP into a different mesophase that resulted in compromised crystal quality and led to poor diffraction.

We explored conversion of the LCP phase from the gel to a liquid-like phase by application of sponge-inducing agents (29) or treatment with a lipase (30). Structures of several membrane proteins have been previously determined using crystals grown in the sponge phase (29, 31–33). We recently described this method and demonstrated that some diffraction data could be obtained from a GPCR crystal (26). In that report, aliquots of GPCR crystals grown in LCP were applied to a TEM grid and covered by a lipase solution, 2-methyl-2,4-pentanediol (MPD), or polyethylene glycol (PEG) on top of the LCP bolus. Conversion of the LCP to the sponge phase was completed in about 1 h. The grid was then observed in the TEM, revealing large areas that were too thick for the electron beam to penetrate. Small crystalline wedges sticking out of the thick LCP matrix were identified. These crystalline wedges appeared dehydrated and only diffracted to around 4- to 5-Å resolution and lasted for just a few exposures before they were destroyed by radiation damage. We surmised that the long incubation time for conversion of the LCP from the gel to the sponge phase may have damaged the fragile crystals, so further modification to this method had to be developed.

The procedure for conversion of the LCP phase from the gel to the sponge phase was modified as follows. Microcrystals of $A_{2A}AR$ were grown in a syringe as described previously (34, 35). The mother liquor surrounding the LCP was ejected from the syringe, leaving behind only the LCP with embedded microcrystals. Small portions of PEG400 100% were added to the LCP stepwise (~5% of the total LCP volume per step) and mixed mechanically back and forth between two syringes until a homogeneous mixture was achieved (Fig. 1 *B*, *Inset*, and *SI Appendix*, Fig. S1). This continued until the gel-like LCP was converted into a liquid-like sponge phase and the syringe could dispense the mixture through a 10-mm, 26-gauge syringe needle by applying only enough force to overcome the traction of the plunger. Microcrystals remained visually intact throughout this procedure. A very small portion (~0.5 μL) of the resultant sponge phase was applied to a TEM grid inside of a vitrification robot at room temperature and 90% humidity. The grid was blotted from the front and then the back, plunged into liquid ethane, and stored under cryogenic conditions.

Vitrified grids with the sponge-$A_{2A}AR$ microcrystals were loaded into a dual-beam FIB/scanning electron microscope (SEM) operating at cryogenic temperatures (36, 37). To our satisfaction, many small crystals were visible on the grid using low-magnification imaging in the FIB/SEM (Fig. 1*B* and *SI Appendix*, Fig. S3). Unlike previous preparations, these crystals were well embedded in a homogeneous layer of a vitrified sponge phase (Fig. 1*B* vs. 1*A*). The crystals were milled using a focused beam of gallium ions into thin lamellae ~200-nm thick (*SI Appendix*, Figs. S2 and S3). The grids were loaded into a Thermo Fisher Titan Krios, where the lamellae prepared in the FIB/SEM were identified using low-magnification montaging. A single diffraction pattern without tilting or rotation was acquired from each lamella to assess their diffraction quality. We observed that all six prepared lamellae diffracted, while four of them diffracted to better than 5 Å. Of these four, one lamellae diffracted to ~4.5 Å, two to ~3.5 Å, and one to better than 3 Å (Fig. 1*C* and *SI Appendix*, Fig. S3). We collected continuous rotation MicroED (18) data from the best four lamellae over wedges of ~70° each (Movie S1).

The MicroED structure of $A_{2A}AR$ was determined from a single nanocrystalline lamella. The total diffracting volume was only about 1 μm^3 (0.2 × 2 × 2 μm), making this ~2 to 3 orders of magnitude smaller than typical GPCR crystals used for structure determination. The integrated data from the best lamella resulted in a dataset to 2.8-Å resolution with an overall $\langle I/\sigma(I)\rangle$ of 7.1 and an overall completeness of ~80%. This dataset was indexed in space group C 2 2 2_1 (#20) with unit cell dimensions of (a, b, c) = 40.0 Å, 180.5 Å,

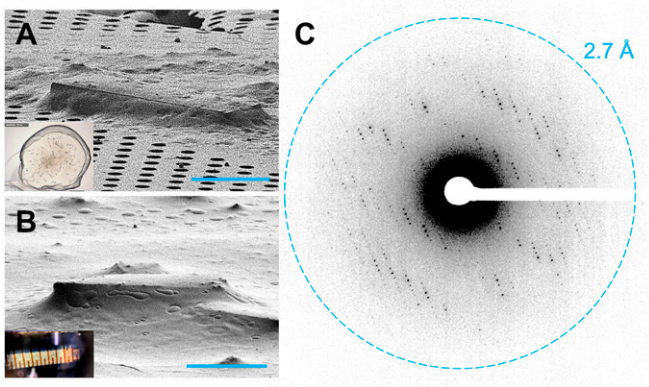

Fig. 1. Preparing GPCR crystals for MicroED data collection. (*A*) An $A_{2A}AR$ crystal looped from a glass sandwich plate and placed on a TEM grid viewed at 18° tilt. (Scale bar, 10 μm.) Typical LCP crystallization drop used for looping GPCR crystals shown (*Inset*). (Magnification: *A*, *Inset*, 15×.) (*B*) An $A_{2A}AR$ crystal from a syringe with microcrystals in the sponge phase. (Scale bar, 10 μm.) Typical syringe with $A_{2A}AR$ crystals grown in LCP after conversion into a sponge phase shown (*Inset*). (Magnification: *B*, *Inset*, 5×.) *A* and *B* were taken using the focused ion-beam inside of the SEM with a beam current of 1.5 pA. (*C*) MicroED data taken from a 200 nm $A_{2A}AR$ crystal lamella, showing spots out to 2.7 Å. A continuous rotation MicroED dataset was collected from this crystal.

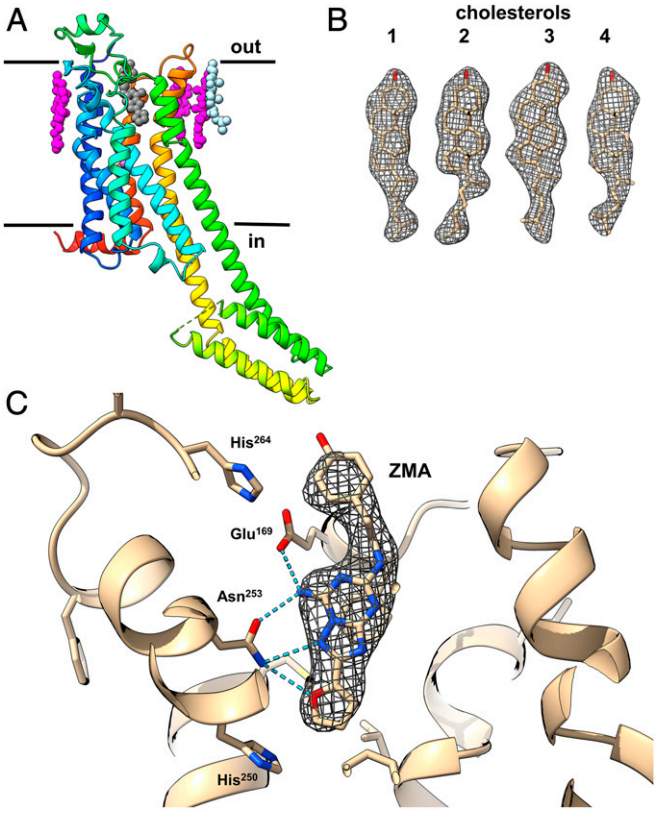

Fig. 2. The structure of $A_{2A}AR$ by MicroED. (*A*) Cartoon representation of the $A_{2A}AR$ GPCR structure depicted in rainbow viewed from the side. The membrane bilayer as indicated. Ligands are shown in sphere representation, where the ZM241385 antagonist is in black, known cholesterol positions in magenta, and the newly determined cholesterol position in light blue. (*B*) Density for the four cholesterol molecules. (*C*) Magnified binding pocket of the ZM241385 antagonist from the region indicated by a circle in *A*. Density is shown around the ligand along with coordination with the protein residues. The $2mF_o$–DF_c maps are contoured at the 1σ level. Maps were generated in Phenix using the default option of filling in missing F_o data with F_c.

139.7 Å, and angles (α, β, γ) = 90°, consistent with prior reports (28, 34). Molecular replacement was conducted using the PDB ID code 4EIY (28) as a search model after removing all ligands and converting all side chains into alanines, resulting in a single, unambiguous solution. Initial maps following molecular replacement showed clear difference peaks where the ZM241385 ligand and ordered lipids were identified in other structures of this protein (28, 34). The molecular replacement solution was refined using electron scattering factors until convergence and side chains were built into the polyalanine backbone (Fig. 2 and *SI Appendix*, Figs. S4–S8). One ZM241385 ligand (ZMA) and four cholesterols were placed in the difference maps (*SI Appendix*, Fig. S5 and Movies S2–S5).

The overall structure of $A_{2A}AR$ is consistent with past reports (Fig. 2 and *SI Appendix*, Fig. S4) (28, 34). The protein folds into a seven-transmembrane (7TM) topology, with the N terminus located on the extracellular side of the membrane and an intracellular helix 8 at the C terminus running parallel to the lipid membrane. The densities for all receptor loops and all four disulfide bonds are well defined (*SI Appendix*, Figs. S6 and S7). TMs 5 and 6 are elongated, protruding well beyond the surface of the cytoplasmic lipid layer where they normally engage the G protein (38). On the extracellular side, four cholesterol molecules were observed per monomer. The antagonist ZM241385 was observed in the orthosteric ligand-binding site inside the 7TM bundle (Fig. 2 and *SI Appendix*, Figs. S4 and S6).

The 2.8-Å resolution structure was refined to an R_{work}/R_{free} of 24.8/28.8%, and good overall geometry (Table 1). Interestingly, we identified one additional cholesterol in this structure, that was interacting with two other cholesterols and Phe183, Phe258 when compared to the previously determined structure of $A_{2A}AR$ (PDB ID code 4EIY). In that structure (4EIY), the site was occupied by an oleic acid rather than a cholesterol (Figs. 2*A*, light blue, and 2*B*) (28). The additional cholesterol identified forms a cluster with two other cholesterols that mediate crystal contacts in plane between two adjacent receptor monomers (Movie S4). The location of the bound antagonist, ZM241385 (ZMA), and coordination to the protein was accurately determined and verified in the omit maps (Fig. 2*C* and *SI Appendix*, Figs. S4 and S5).

MicroED data were collected using an extremely low exposure to minimize radiation damage (39). Recent quantification of radiation damage in MicroED studied the effect of exposure of a crystalline sample to the electron beam. The most sensitive to site-specific damage were disulfide bridges, which showed signs of deterioration even at an average exposure of ~3 $e^{-}Å^{-2}$. The MicroED structure of $A_{2A}AR$ was determined using an average exposure of only 2 $e^{-}Å^{-2}$ (~7.4 MGy) and as expected the density for all four disulfide bridges (C71–C159; C74–C146; C77–C166; C355–C358) remained intact (*SI Appendix*, Fig. S7). This observation suggests that FIB milling did not inflict significant additional radiation damage on the sample.

Because of their rod-like shape, these $A_{2A}AR$ crystals adopt a preferred orientation on the EM grids with a cone of missing reflections along the axis parallel to the incident beam (*SI Appendix*, Fig. S8). Thorough attempts were made to merge additional datasets to increase completeness in the lower-resolution shells of the dataset. Doing so only increased completeness to 84% at 3.8 Å, and 81% at 2.8 Å resolution since all of these datasets were missing similarly oriented wedges (*SI Appendix*, Fig. S8 and Table S1). Attempts at merging also resulted in

Table 1. MicroED crystallographic table for $A_{2A}AR$

	$A_{2A}AR$
Integration	
Wavelength (Å)	0.0197
Resolution range (Å)	37.91–2.794 (2.894–2.794)
Space group	C 2 2 2_1
Unit cell (*a*, *b*, *c*) (Å) (α = β = γ) (°)	40.0, 180.5, 139.7 90
Total reflections (no.)	37,130 (3,584)
Multiplicity	3.7 (3.7)
Completeness (%)	77.07 (72.32)
⟨I/σ(I)⟩	7.46 (1.31)
Wilson B-factor ($Å^2$)	55.66
R_{pim}	0.1879 (0.7499)
$CC_{1/2}$	0.923 (0.15)
Refinement	
R_{work}	0.2482 (0.3354)
R_{free}	0.2881 (0.3852)
No. of nonhydrogen atoms	3,140
Protein residues	390
RMS (bonds) (Å)	0.002
RMS (angles) (°)	0.41
Ramachandran favored (%)	97.41
Ramachandran allowed (%)	2.59
Ramachandran outliers (%)	0
Rotamer outliers (%)	1.94
Clashscore	3.6
Average B-factor ($Å^2$)	43.1
Macromolecules B-factor ($Å^2$)	43.24
Ligands B-factor ($Å^2$)	40.45
Solvent B-factor ($Å^2$)	31.11

degradation of the crystallographic statistics and only slightly increased completeness. Variations in data quality could be due to variations in unit cell parameters, or damage to the crystals during preparation (*SI Appendix*, Table S1). Prior studies have shown that crystals with preferred orientations on the EM grids suffer from a systematic missing cone of data, for which merging data from additional crystals cannot compensate (40, 41). Despite the preferred orientation, a single A_{2A}AR lamella yielded ∼80% completeness and a high-quality density map and structure to 2.8-Å resolution (*SI Appendix*, Figs. S4–S7).

The structure of A_{2A}AR was previously determined at better than 2-Å resolution using XFEL and synchrotron radiation (28, 34). In the case of XFEL, a dataset was assembled from 72,735 single-orientation snapshots from crystals with an average volume of 50 μm^3 per crystal (34), while in the case of synchrotron radiation, data were collected from 55 crystals with an average volume of 1,800 μm^3 per crystal (28). The MicroED structure presented here was determined from a single crystal lamella using less than ∼1 μm^3 volume. This suggests a significant advantage in both the number and size of crystallites needed for structure determination of GPCRs and identification of ligands for future experiments. However, it remains to be seen how other GPCR crystals will behave when LCP is converted to the sponge phase. Preparing grids from samples that do not retain order in the sponge phase may be an additional hurdle to overcome in GPCR structure determination by MicroED.

We determined the first MicroED structure of a GPCR grown in LCP. This structure was determined from a single crystal to 2.8-Å resolution. The crystals were made amenable to MicroED investigation by converting the LCP into the sponge phase and subsequent FIB milling of the microcrystals that were spread on a TEM grid in a humidity-controlled environment. The structure was derived from a single microcrystal milled to a thin lamella only 200-nm thick. The total illuminated crystalline volume for a complete, near-atomic resolution dataset was less than 1 μm^3, a feat essentially impossible using any other crystallographic method. The fully refined structure clearly identified most of the side chains, the bound ligand, and four cholesterols even though they were not included in the search model for molecular replacement, testifying to the high quality of the data obtained. Consistent with the above postulate, we did not observe significant signs of site-specific damage, as all four disulfide bridges appeared intact in the A_{2A}AR density map. The use of sponge phase with microcrystals lays the groundwork for future inquiries of GPCR microcrystals by MicroED. Indeed, it may be prudent to screen for conditions where membrane protein crystals are grown in the sponge phase (42). Of particular interest is the availability of soaking experiments conducted on-grid for structure-based drug discovery (43). This investigation represents a leap forward in the use of MicroED and FIB milling of GPCR microcrystals and has broad implications for how the structures of membrane proteins grown in LCP may be solved in the future using even smaller crystals.

Materials and Methods

Protein Production. Expression and purification of A_{2A}AR, containing BRIL fusion protein in the third intracellular loop and a C-terminal truncation of residues 317 to 412 (A_{2A}AR-BRIL-ΔC), were done as previously described (34).

Crystallization. Purified and concentrated to 30-mg/mL protein samples of A_{2A}AR-BRIL-ΔC in complex with ZM241385 were reconstituted into LCP by mixing with molten lipid using a syringe mixer (44). The protein–LCP mixture contained 40% (wt/wt) protein solution, 54% (wt/wt) monoolein (Sigma), and 6% (wt/wt) cholesterol (Sigma). Crystals for MicroED data collection were obtained in 96-well glass sandwich plates (Marienfeld) and in Hamilton gas-tight syringes similarly to refs. 34, 35, and 44. Precipitant solution contained 50 to 75 mM sodium thiocyanate, 100 mM sodium citrate pH 4.8, 28% (vol/vol) PEG 400, and 2% (vol/vol) 2,5-hexanediol. Crystals appeared in 24 h and reached maximum size of 30 to 50 μm in plates and 10 to 20 μm in syringes within 5 d.

Grid Preparation for MicroED. All experiments used Quantifoil Cu200 R2/2 holey carbon grids. All grids were glow-discharged immediately before use. Samples were initially made using crystals grown in glass sandwich plates as described previously (44). After cracking open the glass, a portion of the LCP bolus containing a large group of crystals was picked up by a 100 μm MiTeGen dual thickness micromount and then carefully transferred to a glow-discharged grid. The transfer was done by gently sliding the loop along the surface of the grid in an attempt to spread out LCP without breaking the carbon foil. This process was modified to include a humidifier to keep the crystals hydrated during the looping process, but ultimately resulted in grids with ice too thick to identify crystals or grid bars. Samples of A_{2A}AR-BRIL-ΔC crystals grown in syringes were used to convert LCP into a sponge phase. For this purpose, the liquid solutions were carefully removed from three syringes and the remaining LCP with embedded microcrystals was consolidated into one syringe (∼20 μL of LCP). Approximately 1 μL of 100% PEG 400 was added into a clean syringe and mixed with the LCP sample by moving it back and forth between two syringes through a coupler containing a 22-gauge needle until homogeneity. The process of adding PEG 400 was repeated several times until the gel-like LCP is converted into a liquid-like sponge phase that could be ejected from a 26-gauge needle without applying any extensive force. Approximately 0.5 to 1 μL of this sponge phase with microcrystals was placed on a TEM grid inside of a Leica GP2 cryo plunger. The sample chamber was held at 20 °C and 90% humidity. The grid was gently blotted from the front for 5 s, the back for 5 s, and then vitrified by plunging into liquid ethane. Grids were stored in liquid nitrogen until use.

FIB Milling and SEM Imaging. All FIB/SEM experiments were conducted on a Thermo Fisher Aquilos dual beam FIB/SEM as described previously (36, 43, 45). A thick layer of sputter-coated platinum ∼500-nm thick was deposited on the grids to protect the samples from the damaging gallium beam. Individual grids were screened using a single low-magnification image in the SEM. If the grid was not destroyed and the grid bars were visible through the LCP or sponge phase matrix, an all-grid map was taken in the MAPS (Thermo Fisher) software. Achieving this thin layer of lipidic meshophase without destroying the grids is challenging and can often take multiple rounds of grid optimization. Lamella sites were identified in the SEM map and crystals were verified by imaging at grazing incidence in the FIB. Select crystals were milled as described previously (22, 36, 37, 45, 46). Briefly, crystals were adjusted to eucentric height. Trenches were milled away from the crystals at an angle of 35° to determine the thickness of the underlying LCP or sponge phase material. After trenching, areas of the crystal were removed from either the top or bottom using the ion beam. As the crystal was thinned, the current of the ion-beam was lowered. When the lamella thickness was ∼300 nm, the lamella was slowly polished using a 10-pA current until a final thickness of ∼200 nm was achieved.

MicroED Data Collection, Structure Determination, and Refinement. Continuous rotation MicroED data were collected as described previously (18, 39, 47). Grids with milled crystals were transferred from the Thermo Fisher Aquilos dual beam FIB/SEM and into a Thermo Fisher Titan Krios TEM. The Krios was cryogenically cooled to liquid nitrogen temperatures and operated at an accelerating voltage of 300 kV, corresponding to an electron wavelength of 0.0197 Å. Typically, about 80% of the lamellae created in the FIB/SEM survived the transfer steps between the two instruments. All MicroED data were collected on a Thermo Fisher CetaD 16M CMOS detector. The data were collected at a camera length 1,900 mm, corresponding to a calibrated crystal to detector distance of 3,491 mm after postcolumn magnification. Lamellae were identified in low-magnification montages, where they were apparent as white stripes against an otherwise black background. Identified lamellae were brought to eucentric height and screened for diffraction by taking a 1-s exposure of the lamella in diffraction mode prior to a full data collection. Suitably well-diffracting lamellae were isolated using a selected area aperture measuring ∼2 μm in diameter to reduce background noise from the surrounding areas. Five of seven lamella (70%) yielded diffraction, while three of those gave diffraction better than ∼3.5-Å resolution. MicroED data were collected using an exposure rate of ∼0.01 $e^- Å^{-2} s^{-1}$, in wedges of 0.6°, where the detector was readout every 3 s, while the stage was rotating at 0.2° s^{-1}. Data were collected as MRC stacks of images and converted to SMV format, as described previously (36, 48). The data were indexed, integrated, scaled, and merged in DIALS (49, 50).

The structure was determined by molecular replacement in Phaser (51) using the PDB ID code 4EIY (28) as a search model after removing all ligands

and converting all side chains into alanines. The structure was refined iteratively in phenix.refine (52) using electron scattering factors and visual inspection and model building in Coot (53) until convergence.

Figures and Graphic Creation. Figures were arranged in Microsoft PowerPoint. Structural models and maps were created using ChimeraX (54). Maps were generated using F_{calc} for missing F values unless otherwise specified.

Human and Animal Models. No human or animal models were used in this study.

Data Availability. Materials and reagents will be made available upon reasonable request to the corresponding author. The structure factors and coordinates for the A_{2A}AR structure are deposited in the Protein Data Bank (PDB ID code 7RM5), and the associated maps are deposited in the Electron Microscopy Data Bank (EMDB) (accession no. EMD-24551).

ACKNOWLEDGMENTS. This study was supported by NIH grants (P41GM136508 to T.G.; R35 GM127086 to V.C.; and R01GM124152 to B.L.N.). The T.G. laboratory is supported by funds from the Howard Hughes Medical Institute.

1. M. C. Lagerström, H. B. Schiöth, Structural diversity of G protein-coupled receptors and significance for drug discovery. *Nat. Rev. Drug Discov.* **7**, 339–357 (2008).
2. V. Katritch, V. Cherezov, R. C. Stevens, Structure-function of the G protein-coupled receptor superfamily. *Annu. Rev. Pharmacol. Toxicol.* **53**, 531–556 (2013).
3. B. C. Heng, D. Aubel, M. Fussenegger, An overview of the diverse roles of G-protein coupled receptors (GPCRs) in the pathophysiology of various human diseases. *Biotechnol. Adv.* **31**, 1676–1694 (2013).
4. K. Sriram, P. A. Insel, G protein-coupled receptors as targets for approved drugs: How many targets and how many drugs? *Mol. Pharmacol.* **93**, 251–258 (2018).
5. B. B. Fredholm, A. P. IJzerman, K. A. Jacobson, J. Linden, C. E. Müller, International Union of Basic and Clinical Pharmacology. LXXXI. Nomenclature and classification of adenosine receptors—An update. *Pharmacol. Rev.* **63**, 1–34 (2011).
6. R. Franco, G. Navarro, Adenosine A_{2A} receptor antagonists in neurodegenerative diseases: Huge potential and huge challenges. *Front. Psychiatry* **9**, 68 (2018).
7. M. Congreve, G. A. Brown, A. Borodovsky, M. L. Lamb, Targeting adenosine A_{2A} receptor antagonism for treatment of cancer. *Expert Opin. Drug Discov.* **13**, 997–1003 (2018).
8. K. Lundstrom, An overview on GPCRs and drug discovery: Structure-based drug design and structural biology on GPCRs. *G Protein-Coupled Receptors in Drug Discovery* **552**, 51–66 (2009).
9. A. Mishin *et al*., An outlook on using serial femtosecond crystallography in drug discovery. *Expert Opin. Drug Discov.* **14**, 933–945 (2019).
10. A. Ishchenko, C. Gati, V. Cherezov, Structural biology of G protein-coupled receptors: New opportunities from XFELs and cryoEM. *Curr. Opin. Struct. Biol.* **51**, 44–52 (2018).
11. H. A. Safdari, S. Pandey, A. K. Shukla, S. Dutta, Illuminating GPCR signaling by cryo-EM. *Trends Cell Biol.* **28**, 591–594 (2018).
12. E. M. Landau, J. P. Rosenbusch, Lipidic cubic phases: A novel concept for the crystallization of membrane proteins. *Proc. Natl. Acad. Sci. U.S.A.* **93**, 14532–14535 (1996).
13. V. Cherezov, Lipidic cubic phase technologies for membrane protein structural studies. *Curr. Opin. Struct. Biol.* **21**, 559–566 (2011).
14. A. Ishchenko *et al*., Toward G protein-coupled receptor structure-based drug design using X-ray lasers. *IUCrJ* **6**, 1106–1119 (2019).
15. U. Weierstall *et al*., Lipidic cubic phase injector facilitates membrane protein serial femtosecond crystallography. *Nat. Commun.* **5**, 3309 (2014).
16. W. Liu *et al*., Serial femtosecond crystallography of G protein-coupled receptors. *Science* **342**, 1521–1524 (2013).
17. D. Shi, B. L. Nannenga, M. G. Iadanza, T. Gonen, Three-dimensional electron crystallography of protein microcrystals. *eLife* **2**, e01345 (2013).
18. B. L. Nannenga, D. Shi, A. G. W. Leslie, T. Gonen, High-resolution structure determination by continuous-rotation data collection in MicroED. *Nat. Methods* **11**, 927–930 (2014).
19. C. G. Jones *et al*., The cryoEM method MicroED as a powerful tool for small molecule structure determination. *ACS Cent. Sci.* **4**, 1587–1592 (2018).
20. S. Liu, T. Gonen, MicroED structure of the NaK ion channel reveals a Na^+ partition process into the selectivity filter. *Commun. Biol.* **1**, 38 (2018).
21. K. Yonekura, K. Kato, M. Ogasawara, M. Tomita, C. Toyoshima, Electron crystallography of ultrathin 3D protein crystals: Atomic model with charges. *Proc. Natl. Acad. Sci. U.S.A.* **112**, 3368–3373 (2015).
22. M. W. Martynowycz, F. Khan, J. Hattne, J. Abramson, T. Gonen, MicroED structure of lipid-embedded mammalian mitochondrial voltage-dependent anion channel. *Proc. Natl. Acad. Sci. U.S.A.* **117**, 32380–32385 (2020).
23. M. Gallagher-Jones *et al*., Sub-ångström cryo-EM structure of a prion protofibril reveals a polar clasp. *Nat. Struct. Mol. Biol.* **25**, 131–134 (2018).
24. T. Gruene *et al*., Rapid structure determination of microcrystalline molecular compounds using electron diffraction. *Angew. Chem. Int. Ed. Engl.* **57**, 16313–16317 (2018).
25. M. Dick, N. S. Sarai, M. W. Martynowycz, T. Gonen, F. H. Arnold, Tailoring tryptophan synthase TrpB for selective quaternary carbon bond formation. *J. Am. Chem. Soc.* **141**, 19817–19822 (2019).
26. L. Zhu *et al*., Structure determination from lipidic cubic phase embedded microcrystals by MicroED. *Structure* **28**, 1149–1159.e4 (2020).
27. V. Polovinkin *et al*., Demonstration of electron diffraction from membrane protein crystals grown in a lipidic mesophase after lamella preparation by focused ion beam milling at cryogenic temperatures. *J. Appl. Cryst.* **53**, 1416–1424 (2020).
28. W. Liu *et al*., Structural basis for allosteric regulation of GPCRs by sodium ions. *Science* **337**, 232–236 (2012).
29. V. Cherezov, J. Clogston, M. Z. Papiz, M. Caffrey, Room to move: Crystallizing membrane proteins in swollen lipidic mesophases. *J. Mol. Biol.* **357**, 1605–1618 (2006).
30. P. Nollert, E. M. Landau, Enzymic release of crystals from lipidic cubic phases. *Biochem. Soc. Trans.* **26**, 709–713 (1998).
31. P. Wadsten *et al*., Lipidic sponge phase crystallization of membrane proteins. *J. Mol. Biol.* **364**, 44–53 (2006).
32. G. Selikhanov, T. Fufina, L. Vasilieva, C. Betzel, A. Gabdulkhakov, Novel approaches for the lipid sponge phase crystallization of the *Rhodobacter sphaeroides* photosynthetic reaction center. *IUCrJ* **7**, 1084–1091 (2020).
33. V. Cherezov *et al*., In meso structure of the cobalamin transporter, BtuB, at 1.95 A resolution. *J. Mol. Biol.* **364**, 716–734 (2006).
34. A. Batyuk *et al*., Native phasing of x-ray free-electron laser data for a G protein-coupled receptor. *Sci. Adv.* **2**, e1600292 (2016).
35. W. Liu, A. Ishchenko, V. Cherezov, Preparation of microcrystals in lipidic cubic phase for serial femtosecond crystallography. *Nat. Protoc.* **9**, 2123–2134 (2014).
36. M. W. Martynowycz, W. Zhao, J. Hattne, G. J. Jensen, T. Gonen, Collection of continuous rotation MicroED data from ion beam-milled crystals of any size. *Structure* **27**, 545–548.e2 (2019).
37. H. M. E. Duyvesteyn *et al*., Machining protein microcrystals for structure determination by electron diffraction. *Proc. Natl. Acad. Sci. U.S.A.* **115**, 9569–9573 (2018).
38. J. García-Nafría, Y. Lee, X. Bai, B. Carpenter, C. G. Tate, Cryo-EM structure of the adenosine A_{2A} receptor coupled to an engineered heterotrimeric G protein. *eLife* **7**, e35946 (2018).
39. J. Hattne *et al*., Analysis of global and site-specific radiation damage in cryo-EM. *Structure* **26**, 759–766.e4 (2018).
40. B. L. Nannenga, D. Shi, J. Hattne, F. E. Reyes, T. Gonen, Structure of catalase determined by MicroED. *eLife* **3**, e03600 (2014).
41. R. M. Glaeser, L. Tong, S.-H. Kim, Three-dimensional reconstructions from incomplete data: Interpretability of density maps at "atomic" resolution. *Ultramicroscopy* **27**, 307–318 (1989).
42. A. B. Wöhri *et al*., A lipidic-sponge phase screen for membrane protein crystallization. *Structure* **16**, 1003–1009 (2008).
43. M. W. Martynowycz, T. Gonen, Efficient, high-throughput ligand incorporation into protein microcrystals by on-grid soaking. BioRxiv (2020, https:/doi.org/10.1101/2020.05.25.115246. Accessed 18 August 2020.
44. M. Caffrey, V. Cherezov, Crystallizing membrane proteins using lipidic mesophases. *Nat. Protoc.* **4**, 706–731 (2009).
45. M. W. Martynowycz, W. Zhao, J. Hattne, G. J. Jensen, T. Gonen, Qualitative analyses of polishing and precoating FIB milled crystals for MicroED. *Structure* **27**, 1594–1600.e2 (2019).
46. E. V. Beale *et al*., A workflow for protein structure determination from thin crystal lamella by micro-electron diffraction. *Front. Mol. Biosci.* **7**, 179 (2020).
47. D. Shi *et al*., The collection of MicroED data for macromolecular crystallography. *Nat. Protoc.* **11**, 895–904 (2016).
48. J. Hattne *et al*., MicroED data collection and processing. *Acta Crystallogr. A Found. Adv.* **71**, 353–360 (2015).
49. G. Winter *et al*., *DIALS*: Implementation and evaluation of a new integration package. *Acta Crystallogr. D Struct. Biol.* **74**, 85–97 (2018).
50. M. T. B. Clabbers, T. Gruene, J. M. Parkhurst, J. P. Abrahams, D. G. Waterman, Electron diffraction data processing with *DIALS*. *Acta Crystallogr. D Struct. Biol.* **74**, 506–518 (2018).
51. A. J. McCoy *et al*., *Phaser* crystallographic software. *J. Appl. Cryst.* **40**, 658–674 (2007).
52. P. V. Afonine *et al*., Towards automated crystallographic structure refinement with phenix.refine. *Acta Crystallogr. D Biol. Crystallogr.* **68**, 352–367 (2012).
53. P. Emsley, K. Cowtan, *Coot*: Model-building tools for molecular graphics. *Acta Crystallogr. D Biol. Crystallogr.* **60**, 2126–2132 (2004).
54. T. D. Goddard *et al*., UCSF ChimeraX: Meeting modern challenges in visualization and analysis. *Protein Sci.* **27**, 14–25 (2018).